SPIN FORMABILITY OF HIGH-STRENGTH ALUMINUM ALLOYS FOR AEROSPACE APPLICATIONS

Mary Cecilia Mulvaney, *PhD Candidate,* University of Virginia
James M. Fitz-Gerald, *Advisor,* University of Virginia

Virginia Space Grant Consortium Student Research Conference
April 13, 2023

Abstract

Near-net-shape fabrication of launch vehicle tanks and aircraft fuselages is proposed to increase manufacturing rates of aerospace structures. Currently, cryogenic tank manufacturing relies on multi-piece construction requiring hundreds of meters of welds that increase both structural weight and inspection time. Metallic aircraft fuselages involve installation of tens of thousands of rivets resulting in long assembly times. NASA is pursuing spin and flow forming technologies for manufacturing such structures with minimal assembly. These processes enable domes and stiffened barrels to be fabricated using single-piece construction, offering significant manufacturing rate benefits over conventional methods. However, aluminum alloys with sufficient formability, such as Al 6061, tend to have insufficient strength for aerospace structural applications. In contrast, alloys with higher strength, such as Al 2139 and Al 2050, exhibit insufficient formability during ambient temperature forming. This study investigates the spin formability of competitive 5xxx- and 2xxx-series Al alloys, identifies defects impeding formability, and sheds light on future processing routes for successful forming.

Introduction

Spin and Flow Forming

Spin forming and flow forming are manufacturing processes, typically performed close to ambient temperature, that produce single-piece, axisymmetric parts[1]. Both processes rely on the action of sets of movable rollers on a rotating blank to plastically deform the material. Spin forming begins with a flat preform, which is shaped into curved or cup-shaped articles in free space. The diameter decreases without appreciable changes to the wall thickness. Flow forming typically begins with a cylindrical preform, which is drawn out against a mandrel. The length increases, the wall thickness decreases, and the inner diameter does not change[1,2]. The integrally stiffened cylinder (ISC) process is a category of flow forming that produces one-piece, axially-stiffened barrel sections in a single operation[3-6]. In the current work, the geometry of the mandrel results in sub-scale components that represent a reasonable facsimile of an ISC configuration[6].

NASA Langley Research Center recently acquired a VUD-600 vertical forming machine from WF Maschinenbau[1] for lab-scale research on the spin and flow forming processes. The system, shown in Figure 1, employs two hydraulically-

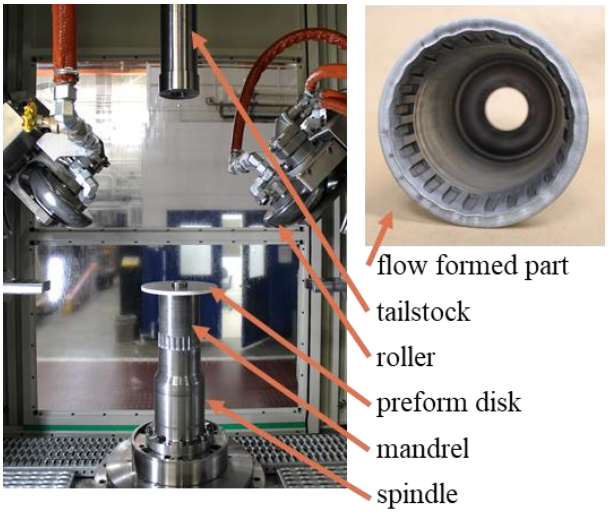

Figure 1: The interior of the VUD-600 forming machine, with major components and a demonstration part highlighted.

[1] *The use of trademarks or names of manufacturers throughout this report is for accurate reporting and does not constitute an official endorsement, either expressed or implied, of such products or manufacturers by the National Aeronautics and Space Administration.*

driven forming rollers and the support of a rotating mandrel and tailstock to deform disk-shaped and cylindrical preforms into spun- and flow-formed articles. Research with the VUD-600 on formability and as-formed properties is expected to transfer to the 3-m-diameter scale to inform alloy selection and ISC stiffener geometries.

Formability

Formability is the measure of the plastic deformation capacity of a material as a function of temperature and stress state. The ambient temperature formability of Al alloys is dependent on composition and temper, but also varies widely for different deformation processes. Generally, higher-strength alloys or temper conditions exhibit lower formability, which often correlates with the decreased ductility. Spin formability is considered to be primarily dependent on the ductility of the material; total elongation (e_{tot}) and area reduction (AR) from tensile tests constitute the most salient predictors[7]. Bylya et al. note that flow formability correlates with *AR*, but also with work hardening coefficient (n) and modulus of resilience (U_r)[8]. All of these material properties can be determined from coupon-scale tensile testing of candidate alloys/tempers. Prior NASA work has had success with ISC fabrication up to the 3-m-diameter scale for the highly-formable Al 6061, but encountered difficulties in forming 2xxx-series Al alloys at scales greater than 0.2-m-diameter[9,10].

In this study, the formability of Al alloys 6061, 5083, 2139, and 2050 in the annealed condition is evaluated through tensile testing and spin forming trials. The goal is to identify factors that impede the spin/flow forming response of the various alloys and highlight processing practices for successful forming.

Materials and Methods

Materials

The materials for this study comprise Al alloys 6061, 5083, 2139, and 2050, with nominal compositions detailed in Table 1. These alloys were selected to cover a range of alloy families, hardening mechanisms, and formability levels.

Al 6061 has the best room temperature formability of the alloys selected for this study. The alloy has significant spin and flow forming heritage, with successful ISCs formed at both the 0.2-m and 3-m diameter scales[6]. Al 6061 only exhibits moderate strength in the -T6 temper, which necessitates the study of other alloys with higher strength potential.

Table 1: Nominal compositions of the Al alloys in this study[11-14].

Element	6061	5083	2139	2050
Ag	–	–	0.40	0.45
Cu	0.28	–	5.0	3.5
Cr	0.20	0.15	–	–
Fe	≤ 0.70	≤ 0.40	≤ 0.15	≤ 0.1
Li	–	–	–	1.0
Mg	1.0	4.4	0.5	0.40
Mn	–	0.70	0.4	0.35
Si	0.60	≤ 0.40	≤ 0.10	≤ 0.08
Zr	–	–	–	0.12
Al	bal.	bal.	bal.	bal.

Al 5083 was selected to assess an alloy where strength is derived from plastic deformation instead of thermal treatment. The alloy has slightly higher strength in the 1/4-hard -H32 temper than Al 6061-T6, rendering Al 5083 an interesting candidate that would not require post-forming heat treatment to attain higher strength. Such a work-hardenable alloy would avoid the issue of distortion of thin-gage, complex-shaped articles that are commonly associated with solutionizing and quenching. Eliminating a heat treatment step would further promote spin forming and ISC-forming processes and enable increased production rates.

Al 2139 and Al 2050 are current generation 2xxx-series alloys that are expected to be less formable than Al 6061, particularly at ambient temperature. Al 2139 was selected for high strength and high damage tolerance[15], which are very beneficial for fuselage applications. Al 2050 was selected for low density, high strength, high damage tolerance, and compatibility with cryogenic fuels for launch vehicles[16], plus forged wing structures for aircraft applications[17].

Spin Forming Trials

The VUD-600 vertical forming machine at NASA was used to conduct the spin forming trials (Figure 1). Disk-shaped preforms with an outer diameter of 220 mm and an inner diameter of 50 mm were prepared for each alloy listed in

Table 1. The Al 6061 and Al 5083 preforms were cut via waterjet from 9.5-mm-thick plate. The Al 2139 and Al 2050 preforms were machined from the center of 25.4-mm-thick plate to a final thickness of 10 mm. The Al 5083 plate was purchased in the fully soft, O-temper condition, while the remaining materials were purchased in various heat-treated conditions and annealed per AMS 2770[18]. The O temper is typically considered to be the most formable condition and was baselined for this study.

The spin forming of the disks into cups was programmed in G-code using five successive downward + upward passes. A generic program that was provided with the VUD-600 was used for spin forming Al 6061. The start and stop positions of the spin forming paths were then modified for the lower-ductility alloys to avoid a necking instability that occurred in the region of tailstock clamping[19]. The two 235-mm-diameter spin forming rollers were set at a 45° angle of declination to complete forming. The rollers were identical with a nose radius of 10 mm and an inlet radius of 70 mm. The spin forming parameters included a spindle rotation speed of 400 rpm, a roller feed rate of 1500 mm/min for the downward passes, and a roller feed rate of 800 mm/min for the upward passes. The rollers were initially set at 180 rpm and allowed to accelerate upon contact with the part. A water-based, flood coolant/lubricant was used to reduce adiabatic heating from the rapid plastic deformation.

Metallurgical and Material Property Analysis

The starting microstructures and grain sizes of the four alloy preforms were characterized via electron backscatter diffraction (EBSD) in a Hitachi S3700 scanning electron microscope (SEM). Cross-sectional images of the plate material along the rolling and normal directions (RD-ND) were taken. The EBSD samples were prepared via flattening and grinding with 600, 800, and 1200 grit SiC paper, polishing with 3-μm and 1-μm diamond slurries, and final polishing with a 0.05-μm alumina suspension. An Oxford EBSD detector was used with a step size ranging from 1.25 μm to 3 μm for the different alloys. Post-processing of the data was performed in the OIM software and followed ASTM E2627[20].

Tensile testing was performed in accordance with ASTM E8[21] using subsize specimens with a gage section measuring 6.35 mm x 6.35 mm x 31.7 mm. Ambient temperature tests were conducted on an MTS Alliance universal testing machine at a crosshead speed of 0.0085 mm/s, achieving strain rates on the order of 10^{-4} s^{-1}. Strain was measured via digital image correlation (DIC) using two 5-megapixel cameras with a 40-ms exposure time and a collection frequency of 1 Hz. The samples were spray-painted with a thin layer of flat white paint, followed by a speckle coating of flat black spray-paint to establish the pattern for DIC analysis. Three 25.4-mm-long virtual extensometers were applied to the gage section data to extract average strain. At least two specimens were tested for each alloy.

Fractography was performed on failed spin formed parts using a Hitachi S3700 SEM in the secondary electron (SE) imaging mode.

Results

Baseline Microstructures

The preform microstructures in the RD-ND plane are shown in the EBSD images in Figure 2, and average grain size statistics are given in Table 2. The Al 6061 and Al 2139 microstructures were very similar, with comparable grain sizes and grain elongation along the RD. The Al 6061 microstructure appeared slightly more elongated than the Al 2139 and Al 5083 microstructures. The Al 5083 microstructure was the most equiaxed and exhibited the smallest grain area, nearly 30 times smaller than that of Al 6061. Al 2050 was the only unrecrystallized alloy, with grains highly elongated in the RD and a large fraction of low-angle grain boundaries (LAGB) compared to the high-angle grain boundaries (HAGB) typical of recrystallized alloys. The strong texture of Al 2050 is expected to

Table 2: Average grain size statistics for the O-temper Al alloy preform RD-ND microstructures.

	6061	**5083**	**2139**	**2050**
Grain area (μm^2)	10400	370	7600	9100
HAGB length/image area (mm^{-1})	37	120	28	69
LAGB length/image area (mm^{-1})	9.9	11	4.1	19

correspond to more anisotropic mechanical properties and spin forming behavior.

Tensile Properties

Representative engineering stress-strain curves for the four alloys in the O-temper condition are shown in Figure 3, and relevant mechanical properties are given in Table 3. As expected, Al 6061 exhibited the lowest strength but the highest ductility. Notably, Al 6061 exhibited almost twice the tensile *AR* compared to the other alloys and an additional 10 percentage points in e_{tot}. This level of ambient temperature tensile ductility supports the well-established formability of Al 6061.

Despite being from different alloy series, Al 5083 and Al 2139 exhibited very similar mechanical properties in the O-temper, with Al 5083 having slightly higher strength and elongation values. Al 2139 and Al 2050 had comparable values of yield strength and ultimate tensile strength. Al 2050 exhibited the lowest ductility, with 30% lower e_{tot} and *AR* than Al 2139. Due to the lower ductility, it is anticipated that Al 2050 would be somewhat harder to form than Al 2139 and significantly more difficult than Al 6061.

Table 3: Average tensile properties of the annealed (O temper) Al preform materials along the RD.

	6061	**5083**	**2139**	**2050**
Yield strength (MPa)	62	133	99	97
Ultimate tensile strength (MPa)	136	298	260	250
Work hardening coefficient, $\boldsymbol{n}$	0.24	0.29	0.31	0.31
Total elongation, $\boldsymbol{e_{tot}}$ (%)	33.8	28.7	27.9	20.0
Area reduction, $\boldsymbol{AR}$ (%)	59	36	38	27

Forming Trial Results

Al 6061 was successfully formed into a cup shape without cracking in a single trial. The successful Al 6061 part, shown in Figure 4, utilized five downward + upward passes to convert the flat disk into a cup shape. The inner mold line (IML), shown in Figure 4b, displayed a rough surface

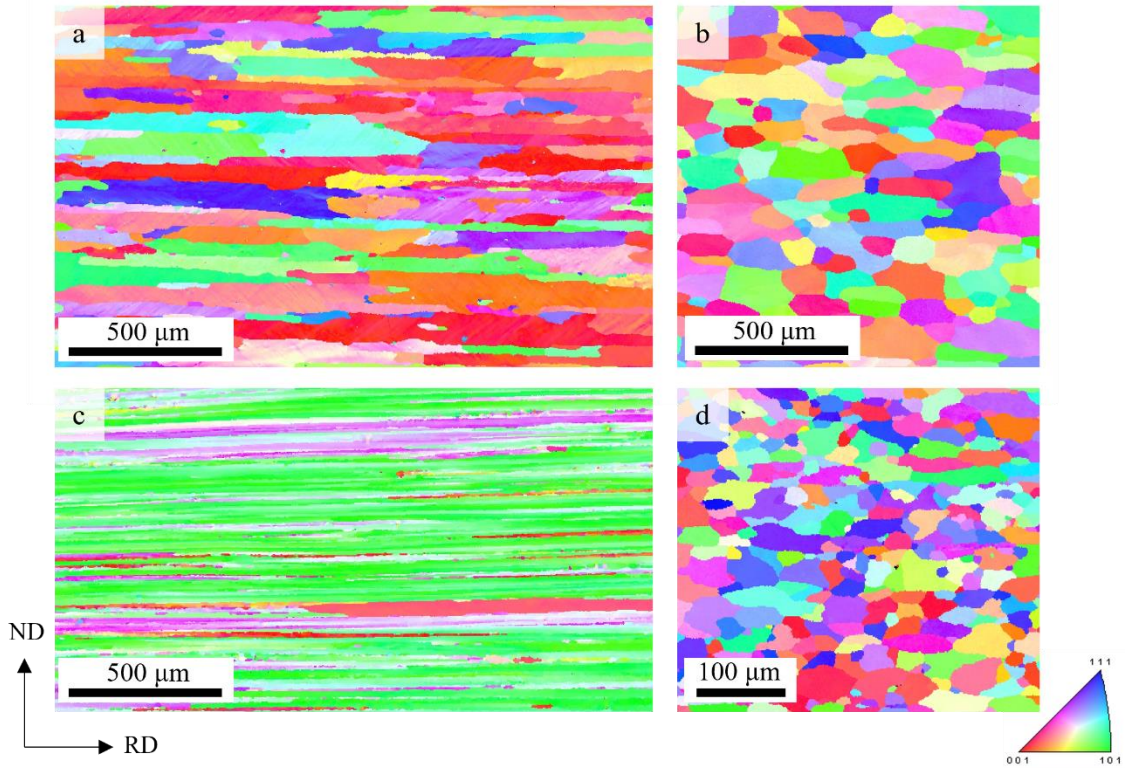

Figure 2: EBSD ND inverse pole figures of the (a) Al 6061, (b) Al 2139, (c) Al 2050, and (d) Al 5083 microstructures showing the varied grain morphologies of the alloys. Note the smaller scale bar for (d).

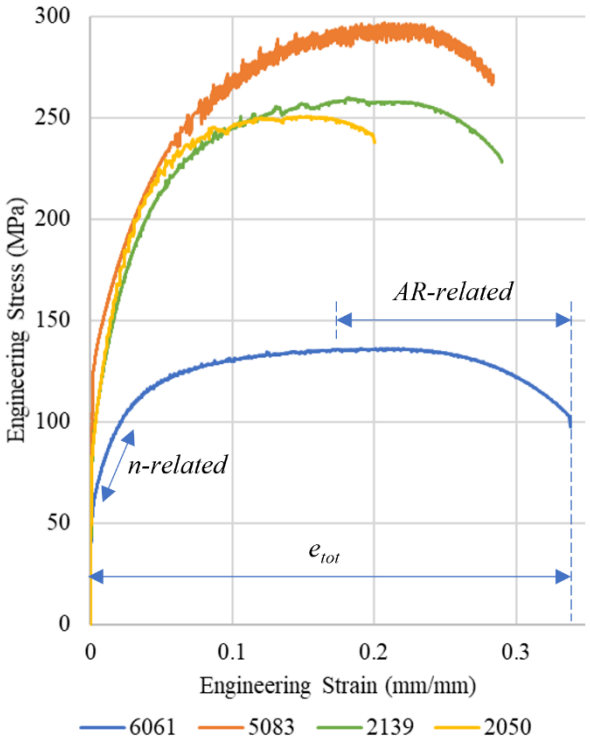

Figure 3: Engineering stress–strain curves for Al alloys 6061, 5083, 2139, and 2050. Select properties of interest are labeled on the Al 6061 curve.

texture, known as "orange peel"[22]. However, no other defects were detected in the part.

Using the forming parameters for Al 6061 as a baseline, the remaining alloys required multiple iterations and forming strategies to form even a partial cup. Severe defects developed during the Al 5083 forming trials, as shown in Figure 5. Early parts failed in shear near the tailstock clamping region due to localized necking. Tensile testing revealed a lower tensile area reduction than Al 6061, which survived the instability during forming[19]. The Al 5083 forming strategy was modified to include "lift-offs" of the rollers from the part between the 1st, 2nd, and 3rd passes, plus modified ending positions for downward passes. These changes resulted in retained thickness near the tailstock clamping region and migrated failure to other susceptible areas in the part. Another failure mode observed was axial cracking (Figure 5a and 5b), which was attributed to notch sensitivity of the material adjacent to the waterjet-cut edges of the blanks.

It was discovered that machining 3-mm radii on the disk edges served to eliminate the edge cracking failure mode. Failures then resulted from microcracks originating in regions of orange peel and linking up to cause flange failure (Figure 5c). The fracture surface of the failed part exhibited "beachmarks," or parallel ridges running through the wall thickness (Figure 5d). Circumferential cracking was also apparent on the outer mold line (OML) of the part (Figure 5e). Intermediate annealing per AMS 2770[18] to restore material ductility and mitigate the orange peel was conducted after every two forming passes until a cup-shaped part was achieved. The resulting part still exhibited orange peel after the final pass and also displayed flaking and lapping on the OML of the part (Figure 5f and 5g).

The Al 2139 material also exhibited severe damage during forming (Figure 6). Similar to the failures noted in the Al 5083, early parts failed in shear at the tailstock clamping region when formed with the baseline Al 6061 code[19]. Roller lift-offs and a sixth spin forming pass were added to avoid the necking instability. The Al 2139 parts also formed considerable orange peel on the IML, with microcracks appearing amidst the orange peel after five passes (Figure 6b). Parts spun to a sixth pass failed from microcracks linking together (Figure 6c and 6d). The fracture surface of the failed part exhibited beachmarks that were more pronounced than those on the Al 5083 fracture surface (Figure 5d). Fractographic examination of the beachmarks revealed that the striations were comprised of alternating regions of fine, ductile dimples (Figure 6e) and shear features (Figure 6f).

Strategies from the Al 5083 and Al 2139 parts were applied to Al 2050, including modified down-pass locations and roller lift-offs (Figure 7). Al 2050 also formed orange peel on the IML. Microcracks developed amidst the orange peel, with larger cracks developing in the transverse direction (TD) of the preform plate and finer cracks along the RD (Figure 7c and 7d). The microcracks in the TD coalesced to result in localized tearing in the TD but not the RD (Figure 7a). The fracture surface of the main crack presented mostly shear features and did not contain the beachmark pattern

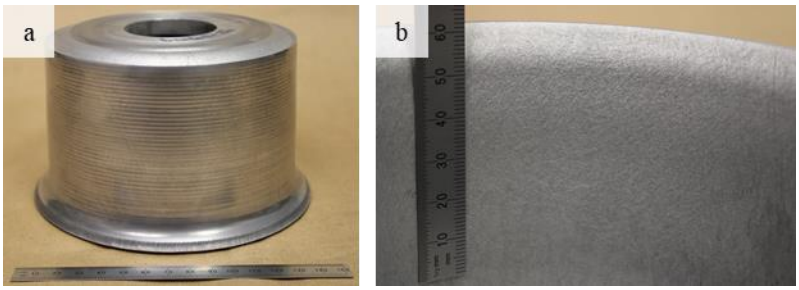

Figure 4: Al 6061 spin forming results showing (a) a successfully spin formed part, and (b) minor orange peel on the IML of the part.

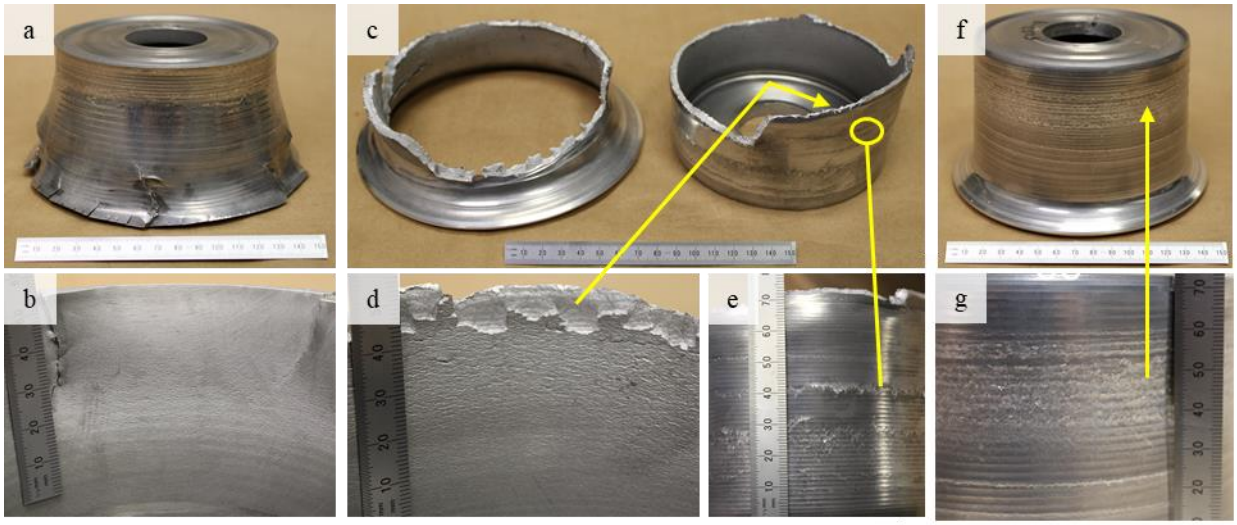

Figure 5: Spin forming results of Al 5083. (a) Failed part showing premature axial cracking emanating from the waterjet-cut edge. (b) IML of the part in (a) showing orange peel and axial tears. (c) Failed Al 5083 part exhibiting (d) orange peel, microcracks, and beachmarks on the IML and (e) circumferential cracks on the OML. (f) Al 5083 part successfully spin formed due to intermediate anneals, with (g) lapping and flaking on the OML.

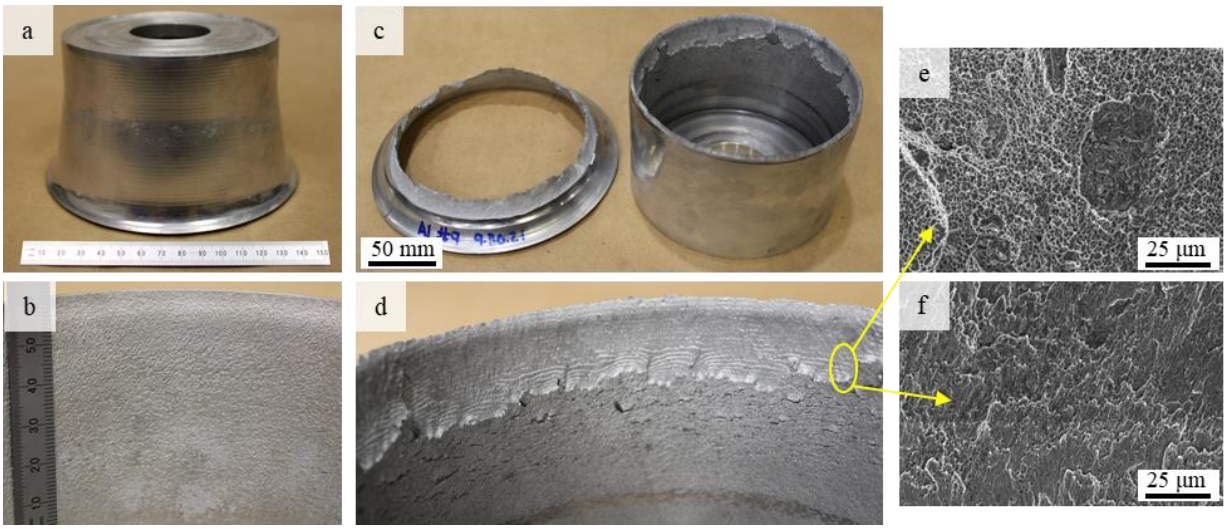

Figure 6: Al 2139 spin forming results, including (a) a part spin formed with 5 of 6 passes, with (b) orange peel and microcracks on the IML. (c) An additional spin forming pass caused flange failure, with (d) beackmarks appearing on the fracture surface. Beachmarks were comprised of alternating regions of (e) dimples and (f) shear features.

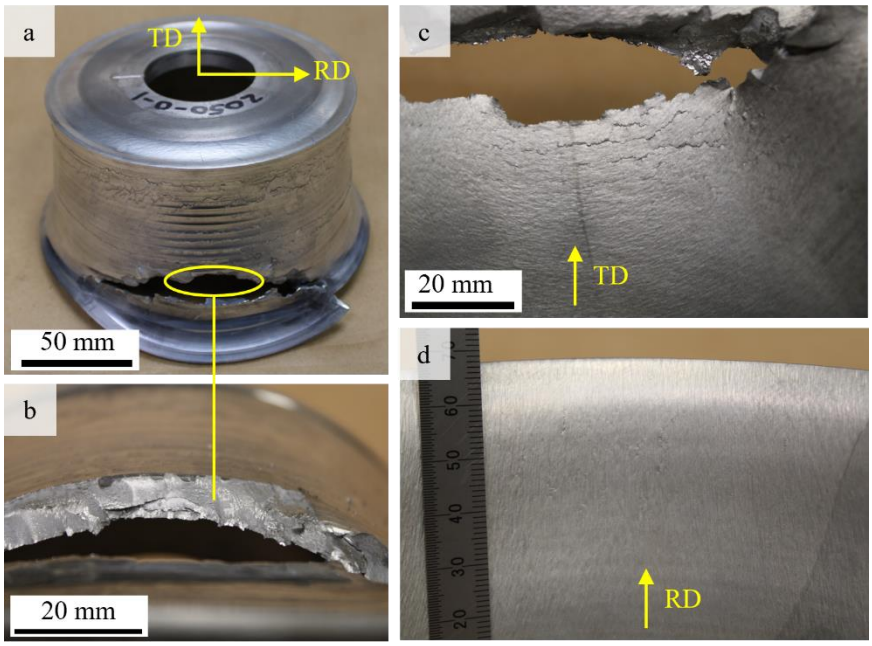

Figure 7: Al 2050 spin formed part exhibiting (a) flange failure, with (b) a fracture surface not showing beachmarks. The orange peel and microcracks differed between (c) the TD and (d) the RD of the original plate.

seen in the Al 5083 and Al 2139 failures (Figure 7b).

Discussion

One significant result from this research was the role that orange peeling played in the premature failure of the Al alloy parts. While the Al 6061 part exhibited orange peel on the IML, it did not experience failure as a result. The 5xxx- and 2xxx-series alloys tested in this study all developed microcracks amidst the orange peel that led to premature part failure. The severity of the orange peel appeared to correlate with increasing work hardening coefficient measured during tensile testing, with Al 6061 showing the least amount of orange peel and Al alloys 2139, 2050, and 5083 showing greater amounts. Intermediate annealing after every two forming passes delayed the development of orange peel in Al 5083, as visual inspection did not reveal orange peel until after the sixth and final forming pass. This delay of orange peel formation may be attributed to the recovery that occurs with annealing that reverses the effects of work hardening. However, intermediate annealing adds additional processing time and is not practical at the 3-m-diameter scale, motivating continued study of Al 5083 with different processing parameters.

The Al 2139 and Al 5083 forming trials revealed that additional forming passes, and thus additional strain, exacerbates orange peel and microcracking. Orange peel occurs exclusively on the IML of the parts because the IML is a free surface that does not have contact with tooling during forming. Furthermore, tensile bending stresses are induced on the IML opposite the roller, as shown in Figure 8, and are linked to orange peel development. Forming strategies that reduce the amount of tensile strain experienced by the IML are expected to decrease the severity of the orange peel. Such strategies may involve down-pass-only roller paths or may alter the “bite” of the roller into the part wall to reduce the magnitude of the tensile stresses on the IML.

The orange peel morphology also tended to correlate with alloy microstructure. The surface roughness of the orange peel on the Al 5083 parts appeared much finer than that of the other alloys, correlating with the smaller grain size. Al 2050 also exhibited microstructure-dependent orange peel. The texturing on the IML of Al 2050 had a ribbon-like appearance, rather than more equiaxed bumps, corresponding to the high-aspect-ratio grains elongated in the RD. The microcracks that developed in the orange peel followed the banded Al 2050 microstructure, running along the RD of the plate and opening wider in the TD than the RD

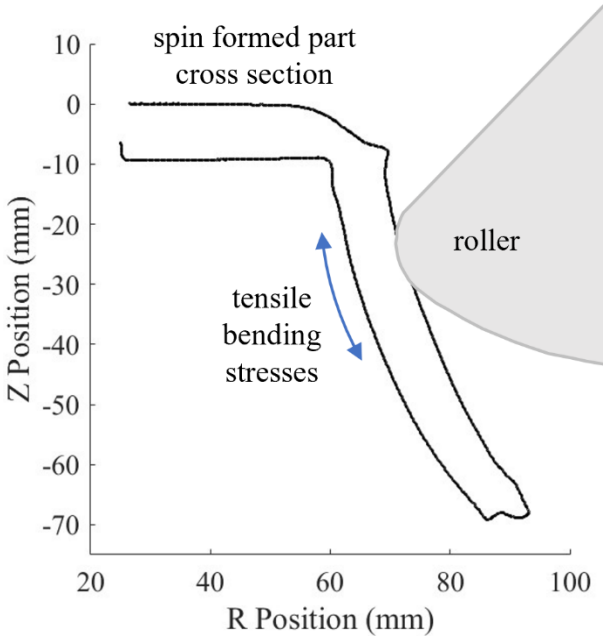

Figure 8: Development of tensile bending stresses on the IML of the part, causing orange peel.

(Figure 7c and 7d). In contrast, the orange peel and microcracks in Al 5083 (Figure 5) and Al 2139 (Figure 6) appeared homogenous around the inner circumference of the part due to the far lower grain aspect ratios.

The fracture surfaces of the failed 5xxx- and 2xxx-series alloy parts also reflect differences in the ductility of the alloys. Al 2139 and Al 5083 exhibited striations on the fracture surfaces, referred to as beachmarks in this study. The beachmarks are reminiscent of markings seen during low cycle fatigue and suggest that flange cracking occurred over multiple revolutions of the part during forming. Fractography in the SEM revealed that the beachmarks were comprised of alternating bands of ductile dimples and shear features (Figure 6e and 6f). In contrast, the fracture surface of Al 2050 showed predominantly shear features and no beachmarks, suggesting a more unstable failure and less material ductility. These observations corroborate the lower ductility of Al 2050 as quantified by the e_{tot} and AR values measured from tensile testing.

The current research reveals that orange peel formation is most detrimental during ambient temperature spin forming of the 5xxx- and 2xxx-series alloys, since all three alloys suffered from orange peeling, cracking during subsequent deformation, and incomplete forming. Solutions that lower work hardening and increase material ductility, such as elevated temperature forming, may enable the successful forming of the high-strength 2xxx-series alloys.

Conclusions

This study investigated the mechanical properties and spin formability of Al alloys 6061, 5083, 2139, and 2050. The following conclusions are drawn:

1. Al 6061 exhibited excellent spin formability due to higher starting ductility and lower work hardening coefficient. Al 6061 was the only alloy that did not develop microcracks in regions of orange peeling.
2. Al 2139 and Al 5083 exhibited similar failures during spin forming, including orange peel and microcracks on the IML and beachmarks on the fracture surface. These correlate with a high work hardening coefficient and a higher e_{tot} than Al 2050.
3. Al 2050 showed preferential orange peel and microcracking in the TD compared to the RD due to the strong preform texture and elongated grains. The fracture surface showed fewer ductile features than those of Al 2139 and Al 5083, consistent with lower e_{tot} and AR properties.
4. Orange peeling was the major impediment to spin forming of the high-strength Al alloys in this study. Elevated temperature forming and down-pass only forming strategies are expected to alleviate orange peel and the ensuing microcracking.

Future Work

A number of exciting avenues remain for this research. Firstly, development of a spin forming schedule without upward passes is expected to reduce tensile bending stresses on the IML. Reduction of the cumulative tensile strain is expected to delay the onset and severity of orange peel, which appeared to be the driver for most failures seen in the higher-strength Al alloys. Additionally, preheating of the Al alloy disks and spin forming without coolant is expected to lower the flow stresses in the material during forming. Lower flow stresses due to elevated temperature

forming should in turn lead to decreased orange peel and increased alloy ductility. Comparison with finite element analysis of the spin forming process will also aid in determining the critical strains at which orange peel and other defects develop.

These formability evaluations for the 2xxx-series Al alloys are ultimately directed towards evaluation of the *flow* formability. Consequently, future work will also entail flow forming trials to determine maximum thickness reduction in a single pass – a measure of flow formability. Additional mechanical testing with compression and notched tensile testing will be performed for comparison with the hypothesis presented by Bylya et al. that tensile testing is the most relevant coupon-scale method for predicting flow formability[9]. This work will culminate in spin and flow formability evaluations of the high-strength 2xxx-series Al alloys and identification of coupon-scale testing to predict formability for screening new candidate alloys.

Acknowledgments

The author gratefully acknowledges the NASA Advanced Air Transport Technology (AATT) project and the Virginia Space Grant Consortium (VSGC) for funding this work. Special thanks to Harold Claytor, Joel Alexa, and Teresa Oneil at NASA Langley Research Center for their assistance in the flow forming trials, and to Wes Tayon and Dave Stegall for their collaboration on the tensile testing. Special thanks to Jim Fitz-Gerald at the University of Virginia and Karen Taminger at NASA Langley Research Center for their mentorship during this research.

References

[1] M. Runge, Spinning and Flow Forming, D.H. Pollitt (trans.), Verlag Moderne Industrie AG, Leifeld GmbH Werkzeugmaschinenbau, Landsberg am Lech, Germany, D-86895, 74 pp., 1993.

[2] G. Ray, D. Yilmaz, M. Fonte, R.P. Keele, Flow Forming, in: S.L. Semiatin (Ed.), ASM Handbook 14A: Metalworking: Bulk Forming, ASM International, 2005: pp. 516–521. https://doi.org/10.31399/asm.hb.v14a.a0004014.

[3] E.K. Hoffman, A.K. Boddorff, K.M. Taminger, C. Mulvaney, D.E. Stegall, Advanced Lightweight Metallic Fuselage Project Manufacturing Trade Study, NASA Technical Memo 2021-0026758. (2022). https://ntrs.nasa.gov/citations/20210026758.

[4] M.C. Stoner, A.R. Hehir, M.L. Ivanco, M.S. Domack, Cost-Benefit Analysis for the Advanced Near Net Shape Technology (ANNST) Method for Fabricating Stiffened Cylinders, NASA Technical Memo 2016-219192. (2016). https://ntrs.nasa.gov/citations/20160006525.

[5] D. Zell, M. Domack, W. Tayon, M. Stachulla, J. Wagner, Developments on Low Cost Manufacturing Methods for Cylindrical Launch Vehicle Structures, in: 67th International Astronautical Congress, Washington DC, USA, 2019.

[6] W.A. Tayon, M.T. Rudd, M.S. Domack, M.W. Hilburger, Development of Advanced Manufacturing Approaches for Single-Piece Launch Vehicle Structures, NASA Technical Memo 2021-0026743. (2022).

[7] R.L. Kegg, A New Test Method for Determination of Spinnability of Metals, Journal of Engineering for Industry. 83:119–124, 1961. https://doi.org/10.1115/1.3664438.

[8] O.I. Bylya, T. Khismatullin, P. Blackwell, R.A. Vasin, The effect of elasto-plastic properties of materials on their formability by flow forming, J. Mater. Process. Technol. 252: 34–44, 2018. https://doi.org/10.1016/j.jmatprotec.2017.09.007.

[9] W.A. Tayon, M.S. Domack, J.A. Wagner, Characterization of 10-ft. Diameter Aluminum Alloy 2219 Integrally Stiffened Cylinders, NASA Technical Memo 2019-220260. (2019). https://ntrs.nasa.gov/citations/20190002739.

[10] M. Domack, J. Wagner, W. Tayon, Integrally Stiffened Cylinder (ISC) Process Development, in: Strategic Interchange Meeting, Leifeld Metal Spinning, Ahlen, Germany, 2015. https://ntrs.nasa.gov/citations/20200007057.

[11] Aerospace Material Specification AMS4468 : Aluminum Alloy, Plate, 5.0Cu - 0.4Mn - 0.5 Mg - 0.4 Ag (2139-T84), Solution Heat Treated, Cold Worked, and Artificially Aged, (2017). https://doi.org/10.4271/AMS4468.

[12] Aerospace Materials Specification AMS4413B: Aluminum Alloy, Plate, 3.5Cu - 1.0Li - 0.40Mg - 0.35Mn - 0.45Ag - 0.12Zr (2050-T84), Solution Treated, Stress Relieved, and Artificially Aged., (2019). https://doi.org/10.4271/AMS4413B.

[13] Aerospace Material Specification AMS4025N : Aluminum Alloy, Sheet and Plate, 1.0Mg-0.60Si-0.28Cu-0.20Cr (6061-O) Annealed, (2020). https://doi.org/10.4271/AMS4025.

[14] Aerospace Material Specification AMS4056H : Aluminum Alloy, Sheet, and Plate - 4.4Mg-0.7Mn-0.15Cr (5083-O) Annealed, (2016). https://doi.org/10.4271/AMS4056.

[15] A. Cho, B. Bes, Damage Tolerance Capability of an Al-Cu-Mg-Ag Alloy (2139), Materials Science Forum. 519–521:603–608, 2006. https://doi.org/10.4028/www.scientific.net/MSF.519-521.603.

[16] M. Niedzinski, The Evolution of Constellium Al-Li Alloys for Space Launch and Crew Module Applications, Light Metal Age, Web. (2019).

[17] N.E. Prasad, A.A. Gokhale, R.J.H. Wanhill, eds., Aluminum-Lithium Alloys, Elsevier, 2014.

[18] Aerospace Material Specification AMS2770R : Heat Treatment of Wrought Aluminum Alloy Parts, (2020). https://doi.org/10.4271/AMS2770R.

[19] M.C. Mulvaney, Flow Formability of Aluminum Alloys for Aerospace Integrally Stiffened Cylinders, in: VSGC Student Research Conference, Newport News, VA, 2022.

[20] ASTM E2627-13: Standard Practice for Determining Average Grain Size Using Electron Backscatter Diffraction (EBSD) in Fully Recrystallized Polycrystalline Materials, ASTM International (2013).

[21] ASTM E8/8M-22: Standard Test Methods for Tension Testing of Metallic Materials, ASTM International (2022).

[22] W.F. Hosford, R.M. Caddell, Metal Forming : Mechanics and Metallurgy, 4th ed., Cambridge University Press, 2014.